

## A *Chandra* STUDY OF THE COMPLEX STRUCTURE IN THE CORE OF 2A 0335+096

P. MAZZOTTA<sup>1,2</sup>, A. EDGE<sup>1</sup>, M. MARKEVITCH<sup>2</sup>

*Submitted to ApJ*

### ABSTRACT

We present a *Chandra* observation of the central ( $r < 200$  kpc) region of the cluster of galaxies 2A 0335+096, rich in interesting phenomena. On large scales ( $r > 40$  kpc), the X-ray surface brightness is symmetric and slightly elliptical. The cluster has a cool dense core; the radial temperature gradient varies with position angle. The radial metallicity profile shows a pronounced central drop and an off-center peak. Similarly to many clusters with dense cores, 2A 0335+096 hosts a cold front at  $r \approx 40$  kpc south of the center. The gas pressure across the front is discontinuous by a factor  $A_P = 1.6 \pm 0.3$ , indicating that the cool core is moving with respect to the ambient gas with a Mach number  $M \approx 0.75 \pm 0.2$ . The central dense region inside the cold front shows an unusual X-ray morphology, which consists of a number of X-ray blobs and/or filaments on scales  $\gtrsim 3$  kpc, along with two prominent X-ray cavities. The X-ray blobs are not correlated with either the optical line emission ( $H\alpha + [NII]$ ), member galaxies or radio emission. Deprojected temperature of the dense blobs is consistent with that of the less dense ambient gas, so these gas phases do not appear to be in thermal pressure equilibrium. An interesting possibility is a significant, unseen non-thermal pressure component in the inter-blob gas, possibly arising from the activity of the central AGN. We discuss two models for the origin of the gas blobs — hydrodynamic instabilities caused by the observed motion of the gas core, or “bubbling” of the core caused by multiple outbursts of the central AGN.

*Subject headings:* galaxies: clusters: general — galaxies: clusters: individual (2A 0335+096) — X-rays: galaxies — cooling flows

### 1. INTRODUCTION

The cores of clusters contain great dynamical complexity. The presence of gas cooling (Fabian 1994), relativistic plasma ejection from the central galaxy (McNamara et al. 2000, Fabian et al. 2000), the action of magnetic fields (Taylor, Fabian & Allen, 2002), possible thermal conduction (Voigt et al. 2002), local star-formation (Allen et al. 1995) and substantial masses of cold ( $T < 30$  K) molecular gas (Edge 2001) all complicate the simple hydrostatic picture.

The launch of *Chandra* and *XMM-Newton* have allowed the cores of clusters to be studied in unprecedented detail spatially and spectrally. These advances have led to a number of important results (e.g., Peterson et al. 2001; Forman et al. 2002, McNamara 2002). The very restrictive limits on low-temperature gas from *XMM-Newton* RGS spectra are forcing us to re-examine some of the basics paradigms of the cooling flows (e.g. Kaastra et al. 2001; Peterson et al. 2001, Tamura et al. 2001, Molendi & Pizzolato 2001). The spatial resolution of *Chandra* can be used to study the brightest, nearby cooling flows to advance greatly our understanding of the processes occurring in these regions. In this paper we present the *Chandra* observation of the Zwicky cluster Zw 0335.1+0956 whose properties may help us to address some of the above issues.

The Zw 0335.1+0956 was first detected as a strong X-ray source by *Ariel-V* (Cooke et al. 1978) and we therefore use the traditional identification of 2A 0335+096 in this paper. 2A 0335+096 is among the brightest 25 clusters in the X-ray sky (Edge et al. 1990). The presence of a cooling flow was noted by Schwartz, Schwarz, & Tucker (1980) and its X-ray properties have been studied extensively over the past two

decades (Singh, Westergaard & Schnopper 1986, 1988; White et al. 1991; Sarazin O’Connell & McNamara 1992; Irwin & Sarazin 1995, Kikuchi et al. 1999). The optical properties of the central galaxy in 2A 0335+096 have been studied in detail (Romanishin & Hintzen 1988; McNamara, O’Connell & Bregman 1990) and the strong, extended optical line emission marks this system out as an atypical elliptical galaxy but a prototypical central galaxy in a cooling flow. A deep, multi-frequency radio study of 2A 0335+096 (Sarazin, Baum & O’Dea 1995) shows a weak, flat-spectrum radio source coincident with the dominant galaxy which is surrounded by an amorphous steep-spectrum ‘mini-halo’. The tentative detection of HI absorption (McNamara, Bregman & O’Connell 1990) and firm detection of CO emission (implying  $2 \times 10^9$   $M_\odot$  of molecular gas) and IRAS 60  $\mu\text{m}$  continuum (Edge 2001) further highlight this cluster as one for detailed study. The implied mass deposition rate from the CO detection is low ( $< 5 M_\odot \text{ yr}^{-1}$ ) if the cold molecular gas found is deposited in the cooling flow.

We use  $H_0 = 70 \text{ km s}^{-1} \text{ kpc}^{-1}$ ,  $\Omega = 0.3$ , and  $\Lambda = 0.7$ , which imply a linear scale of 0.7 kpc per arcsec at the distance of 2A 0335+096 ( $z = 0.0349$ ). Unless specified otherwise, all the errors are at 90% confidence level for one interesting parameter.

### 2. DATA PREPARATION

2A 0335+096 was observed on 06 Sept 2000 with the Advanced CCD Imaging Spectrometer (ACIS) using the back-illuminated chip S3. The total exposure time is 21.4 ksec. In this paper we concentrate on the bright central  $r \lesssim 200$  kpc region of the cluster which lies fully within the ACIS-S3 chip.

Hot pixels, bad columns, chip node boundaries, and events with grades 1, 5, and 7 were excluded from the analysis. We cleaned the observation of background flares following the prescription given in Markevitch et al. (2003). Because chip S3 contains the bright cluster region, we extracted a light

<sup>1</sup> Department of Physics, University of Durham, South Road, Durham DH1 3LE; pasquale.mazzotta@durham.ac.uk

<sup>2</sup> Harvard-Smithsonian Center for Astrophysics, 60 Garden St., Cambridge, MA 02138

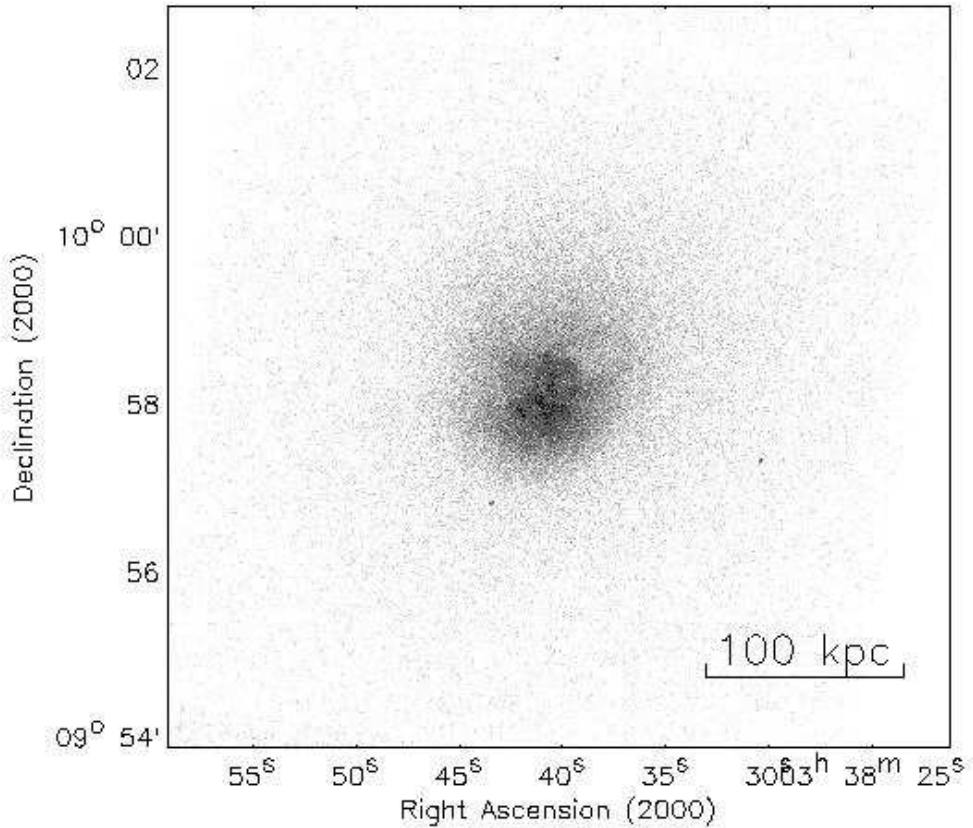


FIG. 1.— Photon image of the central region (ACIS-S3) of 2A 0335+096 in the 0.3-9 keV energy band. The image is background subtracted, vignetting corrected, and binned to  $1''$  pixels. The image shows wealth of substructures in the innermost 50 kpc region. Moreover, it shows two significant surface brightness depressions (cavities) on opposite sides of the X-ray peak in the direction North-West South-East. We also notice a surface brightness edge to the South.

curve for the other backside-illuminated chip S1 in the 2.5–6 keV band, which showed that most of the observation is affected by a mild flare. Because the region of the cluster under study is very bright, we chose a less conservative flare cleaning than is recommended, excluding the time intervals with rates above a factor of 2 of the quiescent rate (taken from the corresponding blank-sky background dataset, Markevitch 2001<sup>3</sup>) instead of the nominal factor 1.2. This resulted in the final exposure of 13.8 ks. During the accepted exposure, the frontside-illuminated chips did not exhibit any background rate increases, therefore the residual background flare is of the “soft” species and can be approximately modeled as described by Markevitch et al. (2003). We fitted the excess background in chip S1 above 2.5 keV with the flare model and included it, rescaled by the respective solid angle, to the cluster fits. The main component of the background was modeled using the above-mentioned quiescent blank-sky dataset, normalized by the rate in the 10–12 keV band (which can be done because the residual flare in our observation is “soft” and does not affect the high-energy rate). The addition of the flare component has a very small effect on the results, because the cluster core is so bright. We therefore ignored the possible (not yet adequately studied) spatial nonuniformity of the flare component.

<sup>3</sup> <http://asc.harvard.edu/> “Instruments and Calibration”, “ACIS”, “ACIS Background”

nent.

### 3. X-RAY IMAGING ANALYSIS

Fig. 1 shows a background subtracted, vignetting corrected image of the central region of the cluster, extracted in the 0.3–9 keV energy band and binned to  $1''$  pixels. The cluster X-ray surface brightness appears to be regular and slightly elliptical at  $r \gtrsim 70''$  (50 kpc). To the South, at about  $60''$  (42 kpc) from the X-ray peak, we notice the presence of a sharp surface brightness edge similar, to those observed in other clusters of galaxies (e.g., Markevitch et al. 2000, Vikhlinin, Markevitch, & Murray 2002a; Mazzotta et al. 2001). Finally, the X-ray image shows complex structure in the innermost  $\approx 50''$  (35 kpc) region. Below we study these features in detail.

#### 3.1. Core structure on larger scale

To investigate the cluster spatial structure, and to compare it with previous studies, we start with the classic approach of fitting the surface brightness with a  $\beta$ -model (Cavaliere, & Fusco-Femiano, 1976). Consistent with previous results, we find that this model does not provide an acceptable fit. Hence, we use a double 2-dimensional  $\beta$ -model defined by:

$$\Sigma = f_{\text{narrow}} + f_{\text{extended}}. \quad (1)$$

The *narrow* and *extended* components of eq. 1 are given by:

$$f(r, r_c, \beta, x_0, y_0, \epsilon, \theta) = A \times \left[ 1 + \left( \frac{r}{r_c} \right)^2 \right]^{-3\beta+1/2}, \quad (2)$$

TABLE 1  
RESULT OF FITTING THE CENTRAL 250'' CLUSTER X-RAY IMAGE WITH A DOUBLE 2D-ELLIPTICAL- $\beta$ -MODEL

Component	$x, y$ (J2000)	$A$ (cnt arcsec $^{-2}$ )	$r_c$ (arcsec)	$\beta$	$\epsilon$	$\theta$ (deg)
Narrow	(03:38:40.9; +09:57:57.5) $\dagger$	$13.2 \pm 0.2$	$85 \pm 1$	$2.45 \pm 0.04$	$0.12 \pm 0.008$	$33 \pm 6$
Extended	(03:38:40.4; +09:58:31.7) $\dagger$	$5.05 \pm 0.06$	$64 \pm 1$	$0.571 \pm 0.004$	$0.13 \pm 0.01$	$34 \pm 4$

$\dagger$ The error of the central position is  $\approx 2''$

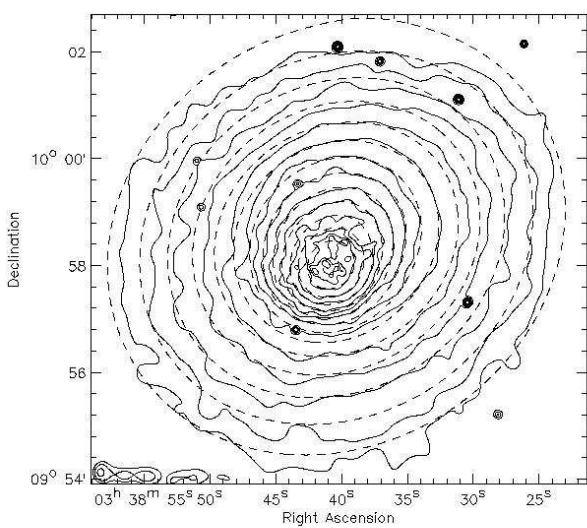


FIG. 2.— Comparison between the X-ray image of 2A 0335+096 and the best fit double  $\beta$ -model. *Continuous lines*: isocontour levels of the cluster image shown in Fig. 1 after adaptive smoothing. The image was smoothed using a Gaussian kernel with a S/N ratio of the signal under the kernel  $\geq 3$ . The levels are spaced by a factor  $\sqrt{2}$ . *Dashed lines*: isocontour levels of the best fit double  $\beta$ -model. The levels are the same as for the X-ray image.

where

$$r(x, y) = \frac{\sqrt{x_{new}^2(1-\epsilon)^2 + y_{new}^2}}{(1-\epsilon)}, \quad (3)$$

and

$$x_{new} = (x - x_o) \cos(\theta) + (y - y_o) \sin(\theta). \quad (4)$$

To perform the fit we use the SHERPA fitting program<sup>4</sup>. The cluster region with  $r > 250''$  and all the strong point sources, together with the regions defined later in §3.3, are masked out. Because the image contains a large number of pixels with few number counts ( $< 20$  cnt) we use the Cash (1979) statistics which, unlike the  $\chi^2$  one, can be applied regardless of the number of counts per bin. The best fit values with their 90% errors are reported in Table 1.

Unlike the  $\chi^2$  statistics, the magnitude of the Cash statistics depends upon the number of bins included in the fit and the values of the data themselves. This means that there is not an easy way to assess from the Cash magnitude how well the model fits the data. To have a qualitative idea of the goodness

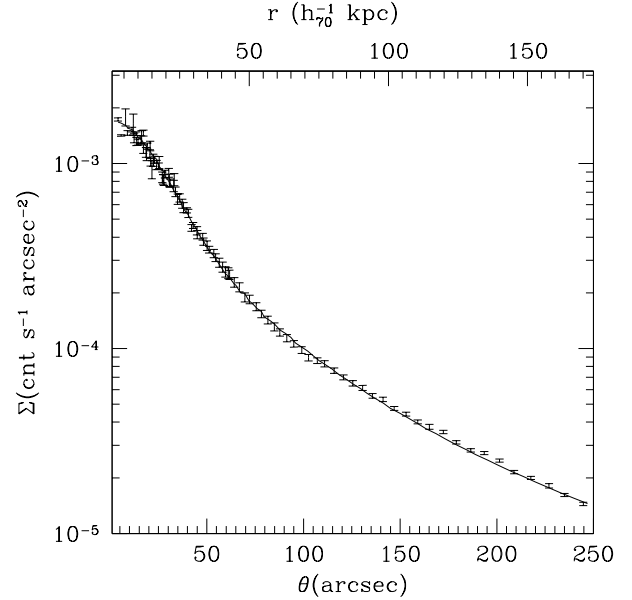


FIG. 3.— Comparison between the surface brightness radial profiles extracted from the X-ray image and the best fit double  $\beta$ -model. To extract the profiles we used concentric ellipses whose center, ellipticity and the orientation where equal to the best fit values of the narrow component of the double  $\beta$ -model. Points with errorbars and lines correspond to the profiles extracted from the X-ray image and the double  $\beta$ -model, respectively.

of the fit, we generate a mock X-ray image using the best fit values of the double  $\beta$ -model and we apply the Poisson scatter to it. Consistent with previous studies, we find that globally the best fit double  $\beta$ -model describes very well the overall cluster structure. This is evident in Fig. 2 where we show the isocontour levels of the model image overlaid to the same isocontour levels of the cluster image after adaptive smoothing. To better illustrate the quality of the fit we also extract the X-ray surface brightness radial profiles in concentric elliptical annuli from both the cluster and the mock images as shown in Fig. 3. The center, the ellipticity and the orientation of each ellipse are set to the best fit values of the narrow component of the double  $\beta$ -model. The figure clearly confirms the good quality of the fit.

The results of the fit reported in Table 1 show that the two spatial components have very different slopes, in particular the narrow component is much steeper than the extended one. We also notice that the profile of the narrow component derived from the *Chandra* data is significantly steeper than the one obtained from the ROSAT PSPC (Kikuchi et al. 1999). The large  $\beta$  value associated with the narrow component indicates that the cluster contains a very compact and dense gas

<sup>4</sup> <http://asc.harvard.edu/> “Data Analysis”, “Introduction”

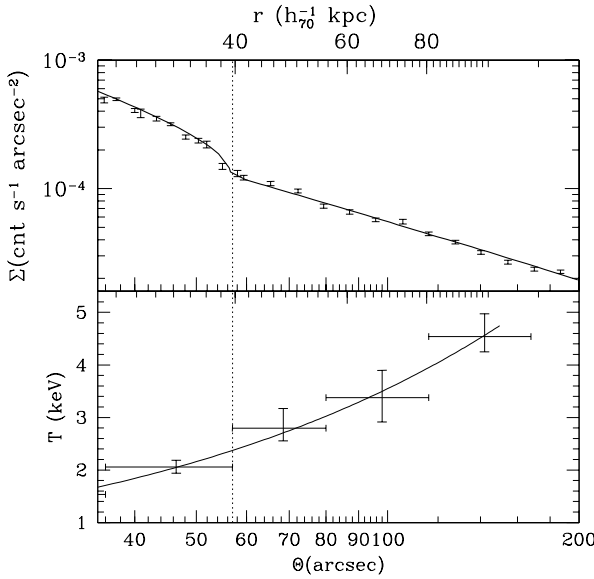


FIG. 4.— *Upper panel*) Cluster surface brightness profile extracted from the  $150^\circ$  to  $210^\circ$  sectors. The continuous line represents the best-fit of the discontinuous two-power law density model. *Lower panel*) Deprojected temperature profile from the  $150^\circ$  to  $210^\circ$  sector. The continuous line is the best-fit of the single power law model.

component with a quite sharp boundary (this is also clearly visible in Fig. 1). On the other hand, the slope of the extended component derived from the *Chandra* data is significantly lower than the value derived from ROSAT (see e.g. Kikuchi et al. 1999, Vikhlinin, Forman, & Jones 1999). Because the *Chandra* result is obtained fitting the cluster surface brightness in a much smaller radial range ( $r < 250''$ ) than the ROSAT one ( $r \lesssim 1200''$ ), this indicates that 2A 0335+096 contains one or more radial breaks at  $r > 250''$ , similar to the ones observed in other clusters like e.g. Hydra-A (David et al. 2001) and Perseus (Fabian et al. 2000).

Finally we note that, although the ellipticity and the orientation are similar, the centroid of the two spatial components are offset by  $\approx 35''$  with the narrow component centroid being further south than the extended one.

Although spatial structure of the cluster is globally well described by a simple double  $\beta$ -model, there are two regions whose structure departs significantly from the best fit model above: i) a  $60^\circ$  wide sector to the south; ii) the innermost  $r < 50''$  cluster region. Below we study in details the spatial structure of these regions.

### 3.2. X-ray “front”

A closer look at Fig. 1 indicates that 2A 0335+096 hosts a surface brightness drop at  $r \approx 50 - 60''$  from the X-ray peak to the south. This X-ray drop spans a sector from  $150$  to  $210$  deg and most closely resembles similar features in other clusters with dense cores and regular morphology on larger linear scales, such as RXJ1720+26 and A1795 (Mazzotta et al. 2001; Markevitch, Vikhlinin, & Mazzotta 2001). To better visualize this feature and to study its nature, we extract the cluster X-ray surface brightness profile within the above sector, using elliptical annuli concentric to the brightness edge. The center, the ellipticity and the orientation of each ellipses are set to the best fit values of the narrow component of the

TABLE 2  
X-RAY FRONT DENSITY, TEMPERATURE, AND PRESSURE BEST FIT VALUES<sup>†</sup>(ERRORS 90% C.L.)

Quantity ( $Q$ )	$s_1$	$s_2$	$A$	$r_{jump}$ (arcsec)
Density ( $n$ )	$-1.36 \pm 0.04$	$-1.20 \pm 0.02$	$1.6 \pm 0.02$	$56.7 \pm 1$
Temperature ( $T$ )	$+0.79 \pm 0.03$	$+0.67 \pm 0.20$	$1.0 \pm 0.20$	...
Pressure ( $P$ )	$-0.57 \pm 0.05$	$-0.53 \pm 0.20$	$1.6 \pm 0.30$	...

<sup>†</sup>Each quantity is modeled using two power-laws with a jump:

$$Q = \begin{cases} (r/r_{jump})^{s_1} & r < r_{jump} \\ A_Q(r/r_{jump})^{s_2} & r > r_{jump} \end{cases}$$

TABLE 3  
SPATIAL AND SPECTRAL PROPERTIES OF THE X-RAY BLOBS

Region	$r_1$ (arcsec)	$r_2$ (arcsec)	net cnts ([0.6-9] keV)	$n_e$ ( $10^{-2} \text{cm}^{-3}$ )	$L_{[0.6-9]}$ $10^{41} \text{erg s}^{-1}$	$t_c$ (10 <sup>8</sup> yr)
1	9.0	4.8	796	8.9	5.8	2.0
2	7.5	5.6	1092	10.0	8.2	1.9
3	5.8	4.6	724	12.7	6.4	2.1
4	6.6	3.7	582	9.4	4.6	2.4
5	7.4	5.1	405	6.4	2.7	2.4
6	8.7	5.1	684	7.6	7.5	4.1
7	4.4	4.3	223	8.3	1.8	3.3
8	5.2	5.2	312	7.2	2.4	2.8

double  $\beta$ -model. The profile is shown in the upper panel of Fig. 4. As extensively shown in previous analysis of cold fronts in clusters of galaxies, the particular shape of the observed surface brightness profile indicates that the density distribution is discontinuous at some radius  $r_{jump}$ .

To estimate the amplitude and the position of the density jump, we fit the profile using a gas density model consisting of two power laws with index  $\alpha_1$  and  $\alpha_2$  and a jump by a factor  $A_n$  at the radius  $r_{jump}$ :

$$Q = \begin{cases} (r/r_{jump})^{\alpha_1} & r < r_{jump} \\ A_n(r/r_{jump})^{\alpha_2} & r > r_{jump} \end{cases} \quad (5)$$

The fit is restricted to radii  $r = 30 - 200''$  to exclude the central region with irregular structure. We assume spherical symmetry. The best fit values together with the 90% confidence level errors are shown in Table 2. The best fit model (which provides a good fit to the data) is shown with a dashed line in the upper panel of Fig. 4.

### 3.3. Core structure on smaller scales

To study the cluster morphology on smaller scales we adaptively smooth the cluster image as shown in Fig. 5. The image was smoothed using the CIAO<sup>5</sup> tool CSMOOTH with a Gaussian kernel and a S/N ratio of the signal under the kernel  $\geq 3$ .

The image clearly shows a very complex structure with a number of blobs of X-ray excess emission. The unsmoothed image shows that these blobs are not necessarily distinct but may form a filamentary structure. Nevertheless, for the purpose of our analysis we assume that the X-ray blobs are ellipsoid. We select 8 regions as shown in Fig. 5. Each ellipse indicates the region where the surface brightness drops by almost a factor two with respect to the peak of its respective X-ray blob. To measure the volume occupied by each blob

<sup>5</sup> <http://asc.harvard.edu/> “Data Analysis”

TABLE 4  
COMPARISON OF SPECTRAL FITS FOR THE INNERMOST 250" REGION

Model	$N_H$ ( $10^{21}$ cm $^{-2}$ )	$T_1$ (keV)	$T_2$ (keV)	$Z/Z_\odot$	$\dot{M}$ ( $M_\odot$ yr $^{-2}$ )	$\chi^2/d.o.f.$
TBABS $\times$ MEKAL	1.6 ( $1.6^{+0.02}_{-0.02}$ )	2.7 ( $2.6^{+0.05}_{-0.05}$ )	...	0.59 ( $0.54^{+0.04}_{-0.04}$ )	...	843/352 (484/297)
TBABS $\times$ [MEKAL+MEKAL]	$1.71^{+0.06}_{-0.05}$ ( $1.71^{+0.08}_{-0.07}$ )	$3.3^{+0.9}_{-0.2}$ ( $3.0^{+0.9}_{-0.2}$ )	$1.4^{+0.3}_{-0.1}$ ( $1.4^{+0.3}_{-0.2}$ )	$0.55^{+0.05}_{-0.05}$ ( $0.53^{+0.06}_{-0.06}$ )	...	643/350 (393/295)
TBABS $\times$ [MEKAL+MKCFLOW]	$2.0^{+0.1}_{-0.1}$ ( $2.0^{+0.1}_{-0.1}$ )	$2.90^{+0.1}_{-0.1}$ ( $2.78^{+0.06}_{-0.06}$ )	...	$0.68^{+0.04}_{-0.04}$ ( $0.60^{+0.04}_{-0.04}$ )	$247^{+37}_{-34}$ ( $192^{+37}_{-34}$ )	658/351 (387/296)
TBABS $\times$ [MEKAL +ZTBABS(MKCFLOW)]	$0.9^{+0.2}_{-0.2}$ <sup>†</sup> ( $1.3^{+0.4}_{-0.4}$ ) <sup>†</sup>	$3.0^{+0.1}_{-0.1}$ ( $2.8^{+0.1}_{-0.1}$ )	...	$0.68^{+0.02}_{-0.02}$ ( $0.61^{+0.05}_{-0.04}$ )	$266^{+35}_{-36}$ ( $249^{+65}_{-60}$ )	658/351 (393/296)

<sup>†</sup>Intrinsic absorption

Values in parentheses are from fits with the excluded 1.4–2.2 keV energy interval.

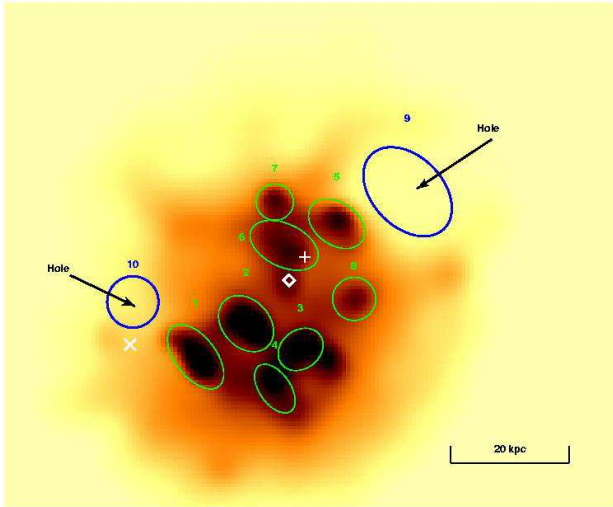


FIG. 5.— Zoom in of Fig. 1 after adaptive smoothing made using a Gaussian kernel with a S/N ratio of the signal under the kernel  $\geq 3$ . The green ellipses labeled from 1 to 8 identify 8 X-ray bright extended regions or blobs. The two blue ellipses, labeled 9 and 10, identify the Western and the Eastern X-ray holes or cavities. The white square and cross, indicate the position of the cluster D galaxy and its companion, respectively. The white X symbol indicate the position of the other cluster central galaxy see (Fig. 11).

we make the simple assumption that the radius of the ellipsoid along the line of sight is equal to the minor radius of the ellipse  $r_2$ . In Table 3 we report the major and the minor radii corresponding to each region shown in Fig. 5. The dimensions of the X-ray blobs span from 4" to 9" (from 2.8 to 6.3 kpc). For each blob we calculate the mean electron density using the following simple procedure: using the method described later in § 4, we extract the spectra from both the blob region and from a cluster region just outside it. Using the latter spectrum as background, we fit the blob spectrum with a thermal model, hence deriving the emission measure. Finally, the gas density is calculated from the emission measure under the simple assumption that it is constant within the blob. The net number of counts and the mean gas densities obtained using the above procedure are reported Table 3. For

completeness in the same table we add the unabsorbed luminosity in the (0.6–9) keV band in the source rest frame and the cooling time (see §4.5 below).

Beside the X-ray blobs, we also note a prominent X-ray hole about 30" (21 kpc) North-West from the X-ray peak, and a less prominent one at  $\approx 40"$  (38 kpc) to the East. To check the statistical significance of the Eastern hole, we extract the count rates from a circular region in the hole ( $r = 6.5"$ ; see Fig. 5) and the count rates in two similar regions to the East and to the West of the depression along the isocontour level defined by the best-fit double  $\beta$ -model. The absorbed flux from the hole is  $\approx 20\%$  lower than the flux from the neighboring regions at a  $4.5\sigma$  confidence level. As shown later in §5, the cluster image may also present other X-ray holes at larger radii. The previous identification of the Eastern hole from ROSAT HRI observations with absorption by a cluster member galaxy by Sarazin et al. (1992, 1995) is not supported with these higher resolution images (see Fig. 5).

#### 4. SPECTRAL ANALYSIS

We use the CIAO software to extract spectra. The spectra are grouped to have a minimum of 20 net counts per bin and fitted using the XSPEC package (Arnaud 1996). The position-dependent RMFs and ARFs are computed and weighted by the X-ray brightness over the corresponding image region using “calcrmf” and “calcarf” tools<sup>6</sup>. To account for the absorption caused by molecular contamination of the ACIS optical blocking filters<sup>7</sup>, all the spectral model we use are multiplied by the ACISABS absorption model<sup>8</sup> that models the above absorption as a function of time since launch. The parameter TDAYS is set to 410, while the others are left to the default values, namely NORM=  $7.22 \cdot 10^{-3}$ , TAUINF= 0.582, TEFOLD= 620, NC= 10, NH= 20, NO= 2, NN= 1.

Spectra are extracted in the 0.6–9.0 keV band in PI channels. At present, the ACIS response is poorly calibrated around the mirror Ir edge, which results in frequently observed signifi-

<sup>6</sup> A. Vikhlinin 2000, (<http://asc.harvard.edu/> “Software Exchange”, “Contributed Software”).

<sup>7</sup> <http://asc.harvard.edu/> “Instrument & Calibration”, “ACIS”, “ACIS QE Degradation”

<sup>8</sup> Chartas & Getman 2002, <http://www.astro.psu.edu/users/chartas/xcontdir/xcont.html>

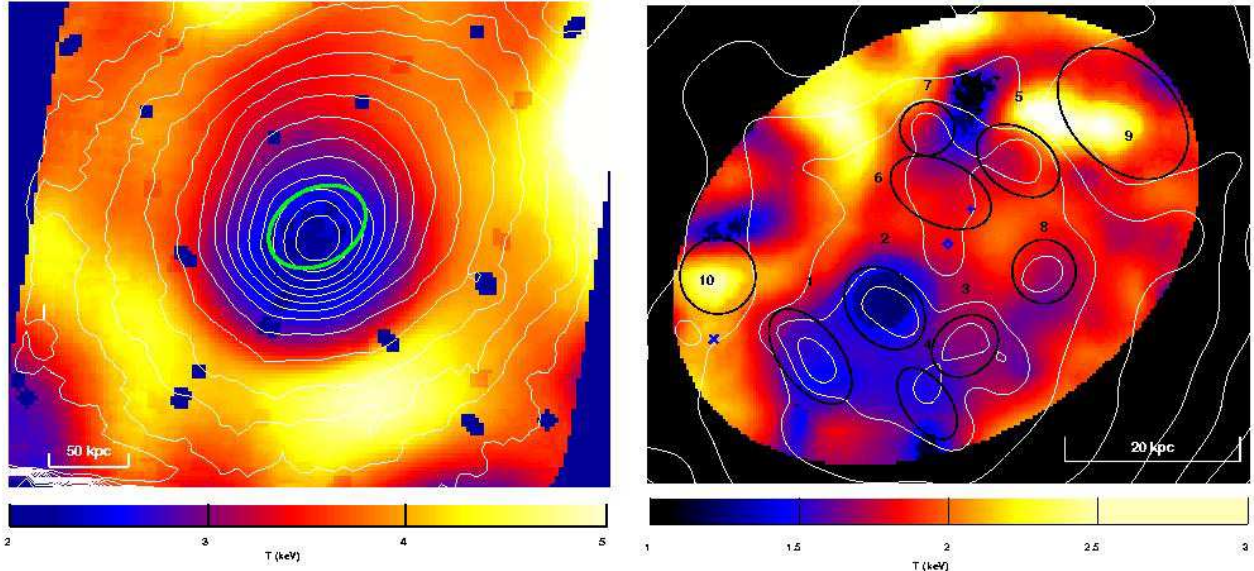


FIG. 6.— Temperature map of 2A 0335+096 overlaid on the 0.3–9 keV ACIS brightness contours. *Left panel*) This temperature map was obtained by smoothing the images using a Gaussian filter with  $\sigma = 15''$ . The green ellipse corresponds to temperature map on the right panel. Blue holes indicate the position of the point sources that were masked out. The isocontours are obtained from the image after a Gaussian smoothing with  $\sigma = 15''$ . Levels are spaced by a factor  $\sqrt{2}$ . *Right panel*) Zoom in, high resolution temperature map from the cluster inside the green ellipse on the left panel. This temperature map was obtained by smoothing the images using a Gaussian filter with  $\sigma = 4''$ . Isolevels are the same as in the continuous lines in Fig 2. The black ellipses labeled from 1 to 10 identify the regions defined in Fig 5. The blue square, cross, and X symbols indicate the position of the galaxies as in Fig. 5.

cant residuals in the 1.4–2.2 keV energy interval and high  $\chi^2$  values. We tried excluding this energy interval and found that the best-fit parameter values and confidence intervals do not change considerably while the  $\chi^2$  values become acceptable, as will be seen below. We therefore elected to use the full spectral range.

#### 4.1. Average Temperature

To determine the average spectral properties of this observation, we extract the overall spectrum from the innermost circular region of  $r = 250''$  (175 kpc) centered on the X-ray peak and fit it with different models as listed in Table 4. In the following the absorption of X-rays due to the interstellar medium has been parametrized using the Tübingen-Boulder model (TBABS in XSPEC v. 11.1; Wilms, Allen & McCray 2000). Furthermore the metallicity refers to the solar photospheric values in Anders & Grevesse (1989). As a first attempt, we use an absorbed single temperature thermal model (TBABS  $\times$  MEKAL; see e.g. Kaasstra, 1992; Liedahl, Osterheld, & Goldstein, 1995; and references therein). We find that this model does not reproduce the spectrum. We also use an absorbed two-temperature model (TBABS  $\times$  [MEKAL+MEKAL]) with the metallicity of the two components linked together. The hydrogen equivalent column density and the temperature, the metallicity, and the normalization of each thermal component are left free to vary. This model provides a much better fit. In particular, if we exclude the energy band near the Ir edge from the spectral analysis, we find that the model is statistically acceptable (see Table 4). We find that the equivalent column density is consistent with the galactic value ( $N_H = 1.78 \times 10^{21} \text{ cm}^{-2}$ ; Dickey & Lockman 1990). The temperatures of both the hot and the cool components, as well as the metallicity, are consistent with the values obtained from the combined analysis of ASCA GIS and SIS spectra extracted from the innermost  $r = 120''$  region (Kikuchi et al. 1999). We finally

fit the spectrum using two models with cooling flows. The first is an absorbed thermal model plus a cooling flow component (TBABS  $\times$  [MEKAL+MKCFLOW]). In the latter we assumed that the cooling flow component itself is intrinsically absorbed by uniformly distributed amount of hydrogen at the cluster redshift (TBABS  $\times$  [MEKAL+ZTBABS(MKCFLOW)], in XSPEC v. 11.1). The higher temperature and metallicity of the cooling flow component are fixed to be equal to the ones of the thermal component. In the first cooling flow we leave the absorption free to vary. In the intrinsically absorbed cooling flow model we fix the overall absorption to the Galactic value and let the intrinsic  $N_H$  free to vary. We find that both models give temperatures, metallicities and the mass deposition rates consistent within the errors. It is worth noting that the cooling flow models give a minimum  $\chi^2$  value similar to the two-temperature model which, as said before, is quite high compared to the degree of freedom (d.o.f.).

#### 4.2. Temperature Map

To determine the temperature map we used the same technique used for A3667 (Vikhlinin, et al. 2001a; Mazzotta, Fusco-Femiano, Vikhlinin 2002). We extracted images in 10 energy bands,  $0.80 - 1.07 - 1.43 - 1.68 - 1.82 - 2.16 - 2.35 - 2.88 - 3.75 - 5.83 - 9.00 \text{ keV}$ , subtracted background, masked out point sources, divided by the vignetting maps and smoothed the final images. We determined the temperature by fitting the 10 energy points to a single-temperature absorbed MEKAL plasma model with metal element abundance fixed at  $Z = 0.6 Z_{\odot}$ . We left as free parameters the equivalent absorption column density, the temperature, and the normalization.

To study the cluster temperature structure at larger radii (where the cluster is less bright), we derive first a relatively low spatial resolution temperature map. This is obtained by smoothing the 10 images above using a Gaussian filter with  $\sigma = 15''$ . The “low-resolution” temperature map, overlaid on

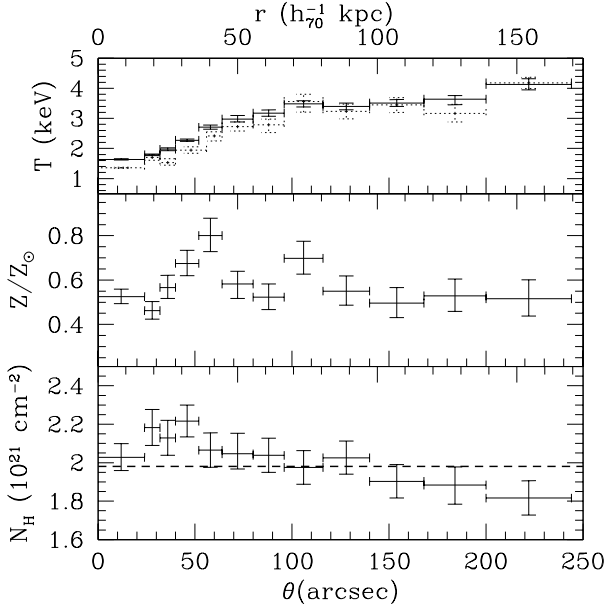


FIG. 7.— Emission weighted temperature, metallicity, and equivalent column density radial profiles of 2A 0335+096 . The spectra are extracted in concentric elliptical annuli. Center, ellipticity and orientation of each ellipses is fixed to the best fit values of the narrow component of the double  $\beta$ -model as shown in Fig. 3. The dotted crosses in the upper panel indicate the results obtained by deprojecting the temperature profiles in the assumption of spherical symmetry. The dotted line in the bottom panel is  $N_H$  value obtained by fitting a constant to the  $N_H$  profile. Error bars are  $1\sigma$  confidence level.

the 0.3-9 kev ACIS brightness contours, is shown in the left panel of Fig. 6. Like the surface brightness, the projected temperature map is not azimuthally symmetric. The gas is substantially cooler in the cluster center and shows a strong positive temperature gradient which varies with position angle. The temperature gradient seems to be higher and lower to the Southern and Northern sectors, respectively. It is interesting to note that the gradient seems to be maximum somewhere in the south sector, where we observe the surface brightness edge.

To study the thermal properties of the X-ray blobs and cavities discussed in §3.3, we produce a second temperature map of the innermost central region using a much higher spatial resolution. This region is identified by the green ellipse in left panel of Fig. 6. The “high-resolution” temperature map, overlaid on the 0.3-9 kev ACIS brightness contours, is shown in the right panel of Fig. 6. The map is obtained by smoothing the 10 images above using a very narrow Gaussian filter with  $\sigma = 4''$ . For clarity we plot ellipses numbered from 1 to 10 corresponding to the 8 X-ray blobs and 2 cavities defined in the §3.3, above (see also Fig. 5). The high-resolution temperature map shows a very complex structure. In particular the cavities and the X-ray blobs seem to have quite different projected temperatures. We discuss this aspect in §4.5 below.

#### 4.3. Radial temperature gradients

We first measure the overall spectral radial properties extracting spectra in concentric elliptical annuli. Center, ellipticity and orientation of each ellipse are fixed to the best fit values of the narrow component of the double  $\beta$ -model as shown in Fig. 3. The radii are choose in order to have  $\approx 20,000$  net counts per spatial bin. Each spectrum is fitted with an absorbed one-temperature MEKAL model. Equivalent hydrogen

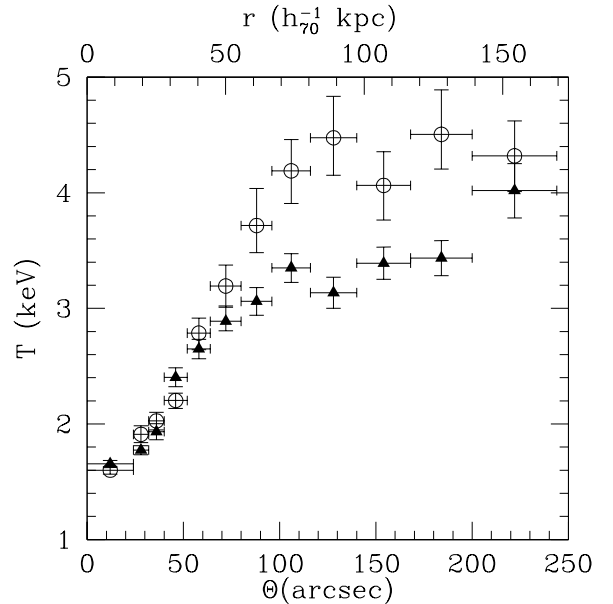


FIG. 8.— Comparison of the temperature profiles extracted from the Northern half (filled triangles) and Southern half (open circles) of the cluster.

column density, temperature, metallicity, and normalization are left free to vary. We get an acceptable fit for all the annuli but the innermost one. The resulting temperature, metallicity, and  $N_H$  profiles, with error bars at  $1\sigma$  level, are shown in the upper, middle, and lower panel of Fig. 7, respectively (errors bars are  $1\sigma$  level). The temperature profile shows a positive gradient within the innermost  $50 - 60h_70^{-1}$  kpc with the temperature that goes from  $\approx 1.5$  keV to  $\approx 3.5$  keV. At larger radii the temperature profile shows a much flatter profile consistent with being constant. Only the last bin at  $150h_70^{-1}$  kpc indicates a possible temperature increment at larger radii. Although the cluster is clearly not spherical symmetric we try to deproject the overall temperature profiles assuming it actually is. The deprojected profile is reported as dotted crosses in the upper panel of Fig. 7. We notice that the deprojected temperature of the innermost bin is  $T = 1.36 \pm 0.02$  keV.

The projected metallicity is consistent with the constant value  $Z \approx 0.5Z_\odot$  at radii  $> 50 - 60h_70^{-1}$  kpc. At lower radii it shows strong positive gradient with a maximum of  $\approx 0.8Z_\odot$  at  $40h_70^{-1}$  kpc. Similar metallicity gradients have been observed in other clusters, e.g. M87 (Molendi & Gastaldello, 2001), Persus (Schmidt, Fabian and Sanders, 2002), Abell 2052 (Blanton, Sarazin, McNamara, 2002), A2199 (Johnstone et al. 2002) and Centaurus (Sanders & Fabian 2002). For some of them, however, it has been shown that the gradient is an artifact induced by the inadequate modeling of the spectra with a single temperature component where a multi-temperature one is actually required. This effect is known as metallicity bias (see Buote 2000). It is interesting to note, however, that if we deprojected the metallicity profile assuming spherical symmetry we find that the profile is consistent with the projected one. This either indicates that the spherical symmetry assumption is inadequate or that the gradient is real. Recently Morris & Fabian (2003) suggested that apparent off-center peaked metallicity profiles may form as result of the thermal evolution of intracluster medium with a non-uniform metal distribution.

Finally, as shown in Fig. 7, panel c), we find that the equivalent column density profile is consistent with a constant value of  $1.98 \times 10^{21} \text{ cm}^{-2}$  which seems to be 10% higher than the galactic value.

As discussed in §4.2, the clusters temperature distribution is strongly asymmetric. To verify the statistical significance of this asymmetry, we extract the spectra using the photons from the Northern or the Southern sectors. Spectra are extracted in the elliptical annuli, with the same binning as before. We find that, although both the abundance and metallicity profiles from the North and the South sectors are consistent within the errors, the temperatures profiles are significantly different. Fig. 8 clearly shows that the temperature gradient in the North sector is shallower than the gradient in the South sector. Moreover, the region of constant temperature in the South sector is a factor 1.3 hotter than that in the North sector.

#### 4.4. Temperature profile of the “front”

In §3.2 we show that the cluster has a surface brightness edge similar to the cold fronts observed in other clusters of galaxies. One peculiar characteristic of these cold fronts is that they have a temperature discontinuity (jump) over the front itself. In this paragraph we study the thermal properties of the X-ray “front” in 2A 0335+096. To do this we estimate the 3D temperature profile of the front by deprojecting the temperature profile from the cluster sector whose angles are from  $150^\circ$  to  $210^\circ$ . The 3D temperature profile is shown in the lower panel of Fig. 4. We notice that the temperature profile has a quite steep gradient. Moreover, unlike the cold fronts observed in other clusters of galaxies, it does not show a clear temperature discontinuity at the front. At first we fit the temperature profile in the range from  $30''$  to  $150''$  with a single power-law model  $T \propto \theta^\delta$ . The model provides a good fit with  $\delta = 0.72 \pm 0.02$ , as shown in Fig. 4. We notice that the data may also be consistent with a small temperature jump at the front. To constrain the amplitude of this possible jump, we fit the data using a two-power law model with a jump  $A_T$  at the position of the front (see eq 5) and we report the result in Table 2. From the table we see that  $A_T = 1 \pm 0.2$ . Using the pressure and the density models above, we calculate the pressure profile near the front region. The best fit model together with the 90% errors are reported in Table 2. The observed density and temperature discontinuity at the front result in corresponding pressure discontinuity of a factor  $A_P = 1.6 \pm 0.3$ .

#### 4.5. Spectral properties of the X-ray blobs and cavities

As discussed in §4.2, the innermost region of 2A 0335+096 has a very complex temperature structure. In particular, the temperature map shows that the cavities and the X-ray blobs have quite different projected temperatures (see Fig. 6). To better study the thermal properties of these structures, we extract spectra for all the elliptical regions shown in the Figure and fit them with an absorbed thermal model. We verify if there is any excess absorption by fixing the metallicity to  $Z=0.6$  solar and letting both  $N_H$  and the temperature to vary freely. As we find that the resulting  $N_H$  values are all consistent with the cluster mean value, we fix  $N_H$  to this value and re-fit the model to measure the temperature. The projected temperatures together with the 90% error bars, are shown in Fig. 9. Consistently with the right panel of Fig. 6, we find that the central X-ray structures have different projected temperatures. In particular we notice that region 1 and 2 are significantly cooler than region 6 and 7. Furthermore,

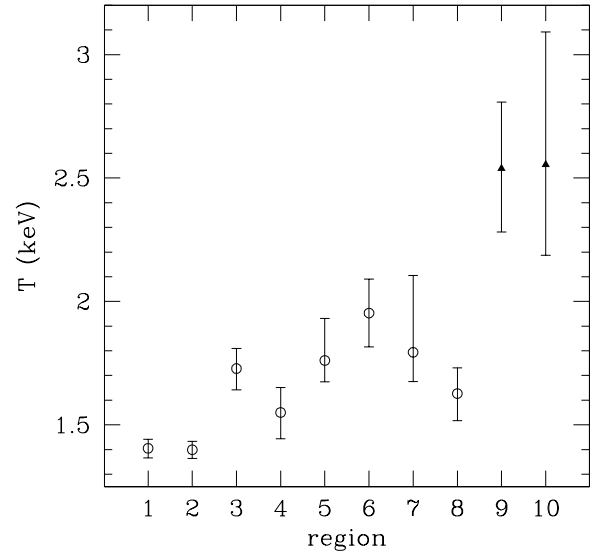


FIG. 9.— Projected temperature from the 8 regions defined in Fig. 5. The two filled triangles give the projected temperature from the Western and Eastern holes, respectively. Error bars are 90% confidence level.

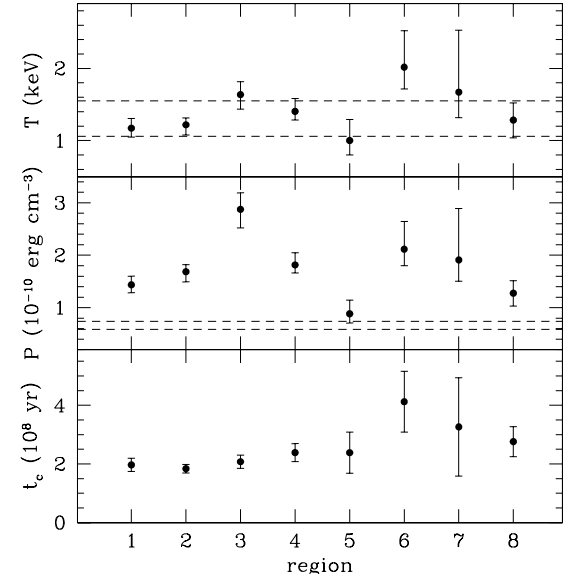


FIG. 10.— *Upper panel*) Deprojected temperature associated with each of the X-ray blobs region defined in Fig. 5. The dashed lines are the 90% error measurement on the deprojected temperature of the ambient gas. *Middle panel*) Thermal pressure associated with the same blobs as in the Upper panel. The dashed lines are the 90% error measurement of the thermal pressure of the ambient gas. *Lower panel*) Cooling time associated with the same blobs as in the Upper panel.

we notice that the holes are significantly hotter than any other X-ray blobs. It is worth noting that the observed higher temperature from the holes is likely to be the result of a projection effect.

Projection could also be responsible for the observed difference in the projected temperature of the X-ray blobs. To verify this hypothesis one should find a way to disentangle the contribution to the spectrum due to the blob itself from

that due to the gas along the line of sight. To perform this task we assume that the contribution to the spectra due to the gas along the line of sight is almost the same within the innermost  $25''$  region (where all the blobs are). This is justified by the fact that the surface brightness profile within this region does not vary more than a factor  $\approx 1.5$ . We then extract a cluster spectrum using a region just outside the blobs that will be used as background for the spectrum of each blob. The first important result of this exercise is that the final spectra clearly shows the presence of Fe-L emission line complex. This proves, without doubt, that the emission from these blobs is indeed mostly, if not all, thermal. We fit these spectra using a single-temperature MEKAL model leaving as a free parameter only the temperature and the normalization. The result is shown in the upper panel of Fig. 10. In the same figure we add, as dashed lines, the 90% error temperature estimate of the ambient gas. This estimate comes from the fit of the blob-free cluster spectrum, used before as background, with a two-temperature MEKAL model with the metallicity of the two thermal components linked together. To compensate our ignorance of the actual 3D cluster structure, we leave the normalization of both thermal components free to vary. We assume that the temperature of the ambient gas coincides with the one of lower temperature component. We believe that this represents a good assumption as the value we find is consistent with the temperature of the innermost bin obtained using a spherical symmetric deprojection model (see upper panel of Fig. 7).

Unlike the emission weighted temperatures, the deprojected ones have a much lower scatter. Furthermore, all regions, but the 6th, have temperatures consistent with the 3D temperature of the ambient gas.

Using the blob density measurements reported in Table 3, it is now possible to estimate the thermal pressure associated with each blob. This is shown in the central panel of Fig. 10. In the same figure we add, as dashed lines, the 90% error ambient pressure. The blobs, except region 5, have thermal pressure values significantly higher than the ambient thermal pressure. This unexpected finding will be discussed below.

Using the temperature and the density of each blob we also estimate their cooling times  $\tau_c \equiv 5P/2\epsilon$ , where  $P$  and  $\epsilon$  are the blob's pressure and the emissivity, respectively. These, together with the 90% error bar, are shown in the lower panel of Fig. 10. We notice that all blobs have similar cooling times which are consistent within the errors (but see region 6). For practical reasons we report also the blob cooling times in column 7 of Table 3.

For completeness we estimate the X-ray blob unabsorbed luminosities in the (0.6-9.0) keV in the source rest frame, as shown in column 6 of Table 3.

##### 5. PROPERTIES AT OTHER WAVELENGTHS

We conclude the analysis of 2A 0335+096 by comparing the cluster properties in the X-rays to those at other wavelengths.

In Fig. 11 we show an HST image of the central region of 2A 0335+096 superposed on contours of the X-ray image after adaptive smoothing. The optical image shows one central D galaxy (PGC 013424, Paturel et al. 1989) with a companion smaller galaxy  $7''$  to the North-West and another elliptical galaxy at  $41''$  to the East. In Fig. 11 the X-ray blobs, defined previously in §3.3 (labeled 1 to 8 in Fig. 5), can be easily identified matching the small quasi-elliptical isocontour regions. Apart from one X-ray blob coincident with the cluster

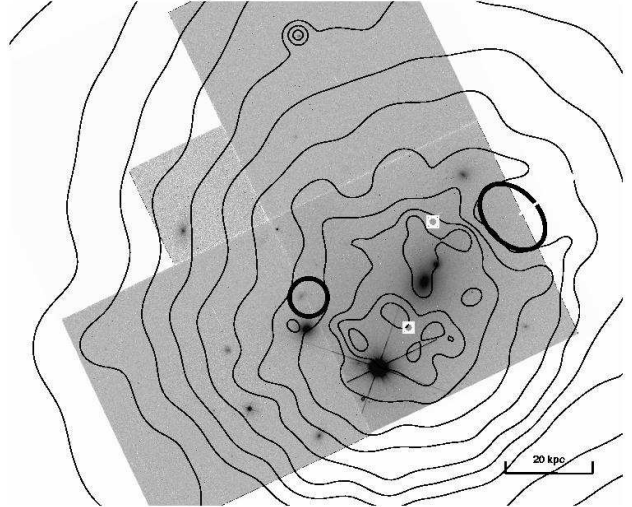


FIG. 11.— HST image of the central region of 2A 0335+096 superposed on contours of the X-ray image after adaptive smoothing. The circles in square symbols indicate the best fit central position of each of the components of the double  $\beta$ -model. The Northern and the Southern symbols indicate the position of the Extended and Narrow component, respectively. The thick ellipses indicate the position of the Western and Eastern holes, respectively. The X-ray excess regions labeled 1 to 8 in Fig. 5 can be easily identified by the small quasi-elliptical isocontour regions. Notice that none of these regions have an optical counterpart.

D galaxy none of the other blobs have optical counterparts. This strongly suggests that the X-ray blobs are produced by some kind of hydrodynamic process.

For completeness in Fig. 11 we report the centroid position of the narrow and extended  $\beta$ -model components. It is worth noting that the D galaxy position does not coincide with either of these centroids but rather lies in between.

The central galaxy of 2A 0335+096 has been found to have a number of peculiar properties over the past 2 decades. Initially it was classified as a Seyfert 1.5 or Liner by Huchra, Wyatt & Davis (1982) but more detailed optical observations by Romanishin & Hintzen (1988) found a very extended optical emission line region ( $H\alpha+[NII]$ ) to the North-East of the galaxy (extended over 30 kpc) and the central regions of the galaxy are anomalously blue indicating recent star-formation (see Fig. 12). Recently a number of authors have shown that some of the extended  $H\alpha$  features observed in the central region of a number of clusters correlate with similar structures of X-ray excess (e.g. A1795, Fabian et al. 2001; RX J0820.9+0752, Bayer-Kim et al. 2002; Virgo, Young, Wilson, & Mundell 2002).

To study the correlation between the X-ray blobs and the line emission in Fig. 12 we show the narrow band  $H\alpha+[NII]$  image from Romanishin & Hintzen (1988) with the X-ray isocontours superimposed. The accuracy of the alignment is better than  $3''$ . There is no direct correlation between the X-ray and  $H\alpha+[NII]$  structures but there is a tendency for the two to lie close to each other. However, the statistical significance of this tendency is difficult to judge. Note the X-ray blobs labeled 1 and 4 lie too close to the saturated star to the South East of the  $H\alpha+[NII]$  image to detect the fainter  $H\alpha+[NII]$  emission.

The radio properties of 2A 0335+096 are also of note. Sarazin et al. (1995) find an amorphous, steep spectrum ( $\alpha \sim -1.4$ ) 'mini-halo' around PGC 013424 which has relatively low radio power compared to other similar sys-

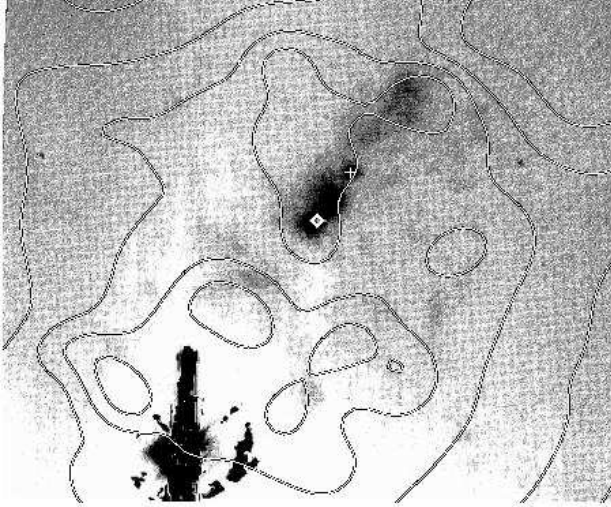


FIG. 12.—  $\text{H}\alpha + [\text{NII}]$  image of the central  $60'' \times 70''$  region of 2A 0335+096 (from Romanishin & Hintzen 1988, Fig. 3) with X-ray contours overlaid. The X-ray contours are the same as in Fig. 11. To better visualize the faintest line features we show the  $\text{H}\alpha + [\text{NII}]$  image in both high and low contrast (left and right panels, respectively). The square and the cross symbols indicate the position of the central D galaxy and its companion, respectively. The X-ray excess region labeled 1 to 8 in Fig. 5 can be easily identified by the small quasi-elliptical isocontour regions. The Western X-ray cavity is located in the upper right hand corner. Note that the large, bright artifact in the lower left of the image is a saturated star.

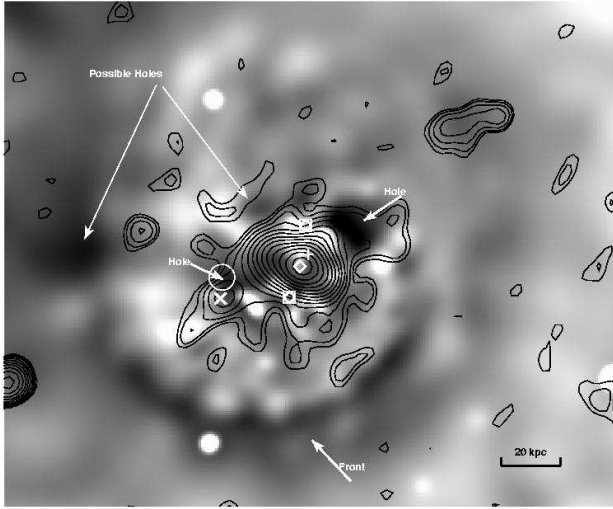
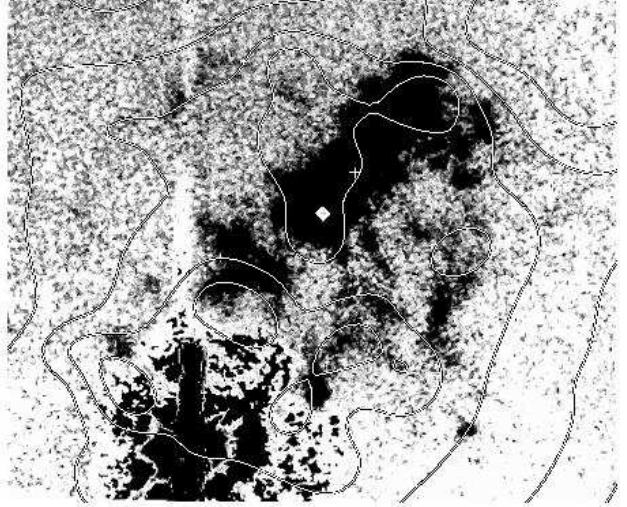


FIG. 13.— Percentile variation of the cluster X-ray image (after adaptive smoothing) with respect to the best fit double  $\beta$ -model superposed on contours of the 1.515 GHz radio image (from Sarazin, Baum, & O'Dea, 1995). The darker and lighter regions indicate negative and positive variation  $\geq |20\%|$ , respectively. The arrows indicate the position of the Western and Eastern holes and the position of the Front. The square and the cross symbols indicate the position of the central D galaxy and its companion while the X symbol indicates the position of the third cluster galaxy in the HST field (see Fig. 11). Finally the circles in squares symbols indicate the best fit central position of each of the components of the double  $\beta$ -model.

tems. Fig. 13 shows the image of the percentile variation  $((\Sigma_{cl} - \Sigma_{mod})/\Sigma_{cl})$  of the cluster X-ray surface brightness  $\Sigma_{cl}$  with respect to the best fit double  $\beta$ -model  $\Sigma_{mod}$ . The isocontours of the VLA 1.5 GHz C+D-array image (resolution  $16''$ ) from Sarazin et al. (1995) are superimposed. The image clearly shows the position of the X-ray front together with the X-ray blobs and the Western and Eastern holes earlier studied in §3.2 and §3.3, respectively. We notice that the mini-radio halo is well within the radius defined by the position of the X-ray front. Unfortunately the spatial resolution of the radio map is insufficient to correlate it with the X-ray

blobs. However, there is some indication that, as observed in other clusters (see McNamara 2002 for a review), both X-ray holes may contain some steep spectrum radio emission which may be ‘relic’ emission from previous radio lobes. Future high resolution, low frequency radio observations will be crucial to linking the radio mini-halo and X-ray structure.

It is worth noting that Fig. 13 also suggests the presence in 2A 0335+096 ghost X-Ray bubbles at larger radii similar the ones observed in other clusters (McNamara 2002). Unfortunately, because of the relatively short exposure, these bubbles are not statistically significant. A deeper X-ray observation is needed to confirm their existence.

## 6. DISCUSSION

The *Chandra* observation of 2A 0335+096 reveals that the core region of this otherwise relaxed cluster is very dynamic.

The cluster image shows an edge-like feature at  $40 - 90$  kpc from the X-ray peak to the south. The edge spans a sector from  $150^\circ$  to  $210^\circ$  from the North.

On smaller scales ( $< 20$  kpc) the cluster image shows a very complex structure with X-ray filaments or blobs. Moreover it shows the presence of two X-ray cavities (see Fig. 5).

The spectral analysis clearly shows that on large scales the cluster temperature distribution is not azimuthally symmetric (see §4.2 and §4.3). Furthermore, the cluster gas temperature reaches its maximum in a region at  $\approx 90$  kpc from the X-ray peak to the south, just beyond the surface brightness edge (Fig. 6). On smaller scales the X-ray blobs have similar temperatures but different pressures.

Below we discuss the results of our analysis and propose possible dynamical models that may explain the observed properties of the core of 2A 0335+096.

### 6.1. Nature of the surface brightness edge: a cold front

In §3.2 we analyze the spatial structure of the X-ray front. We show that the front is well fit by a discontinuous density profile with a density jump at the front of a factor  $\approx 1.6$ . Similar density jumps have been observed by *Chandra* in many clusters, including A2142, A3667, RX J1720+26, A1795. In

those clusters, they are interpreted as sharp boundaries of a dense, cooler gas cloud moving with a speed  $v$  through the hotter and more rarefied ambient gas. The surface brightness edge in 2A 0335+096 appears to be a similar cold front. As discussed by Vikhlinin, et al. 2002a, the pressure profile across the front can be used to determine the Mach number  $M \equiv v_1/c_{s1}$  of the moving cooler gas cloud with respect to the speed of sound in the gas upstream,  $c_{s1}$ .

In Table 2 we show that the pressure jump across the front is  $A_P = 1.6 \pm 0.3$ . This corresponds to a Mach number for the dense central gas cloud of  $M \simeq 0.75 \pm 0.2$  (see e.g. Fig. 6 of Vikhlinin, et al. 2001a). Such subsonic motion of the cool gas cores appears to be very common among the otherwise relaxed clusters with cooling flows (Markevitch, Vikhlinin, & Forman 2002).

## 6.2. X-Ray Blobs

In the analysis above, we identified a number of X-ray blobs most of which are likely to be part of a filamentary structure. As can be seen from Table 3, the blobs are quite dense: their densities range from  $\approx 0.06$ – $0.13$  cm $^{-3}$ . Although the projected spectral properties of the blobs are significantly different (i.e. they have different emission weighted temperatures; see right panel of Fig. 6 and Fig. 9), in §4.5 we show that the temperature of their immediately surrounding ambient gas and the deprojected blob temperatures are consistent within the errors for all but one of the blobs (see upper panel Fig. 10). This is particularly interesting as it implies that the thermal pressure of the blobs is higher than the thermal pressure of the surrounding ambient gas. This finding, however, does not necessarily mean that the blobs are out of pressure equilibrium with the ambient gas as the latter may have extra non-thermal pressure (for example, magnetic fields and/or relativistic electrons ejected from the central AGN). Although at the moment it is not clear which physical processes may be responsible for the formation of the observed substructures, we can safely state that the system is dynamically unstable and the presence of blobs is likely to be a transient phenomenon. We notice that the evolution of the system strongly depends on the total pressure supporting the ambient gas. Below we discuss two extreme possibilities:

1) the ambient gas surrounding the blobs is only supported by thermal pressure and thus the blobs are actually not in pressure equilibrium;

2) the ambient gas, and possibly to some extent the blobs too, are supported by an extra non thermal pressure component such that the blobs and the ambient gas are actually in pressure equilibrium.

In the first case, the blobs are overpressured so we expect them to expand. The expansion time is of the order of the blob's sound crossing time:

$$t_{cross} = 2r_1 \sqrt{\frac{\mu}{\gamma kT}} = 1.7 \times 10^7 \text{ yr} \left( \frac{r_1}{5 \text{ kpc}} \right) \sqrt{\frac{(\mu/0.69)m_p}{(\gamma/1.66)(kT/1.3 \text{ keV})}}, \quad (6)$$

where  $r_1$  is the radius of the blob, and  $\mu$ ,  $m_p$ , and  $\gamma$  are the mean particle weight, the proton mass and the adiabatic index, respectively. Using the linear dimension of the blobs reported in Table 3 we find  $t \approx 1$ – $2 \times 10^7$  yr, which appears to be very short compared with the likely cluster age. Furthermore, the blobs cooling time is  $\approx 10$  times longer than the dynamical time (see lower panel of Fig. 10). Thus, in this first case in which the external gas is not supported by an extra pressure

component, the blobs should expand before their excess pressure is radiated away. Consequently we do not expect to have a significant mass deposition into a cold phase from the blobs.

Conversely, if the blobs are both in thermal and pressure equilibrium with the ambient gas, as in the second case considered above, the blobs are likely to be more stable. Nevertheless, as the blobs are heavier than the ambient gas (they have higher densities), they are expected to sink eventually toward the minimum of the potential well. The time scale  $t_s$  needed by the blobs to reach the cluster center is obviously  $t_s > t_{ff}$ <sup>9</sup>, where  $t_{ff}$  is the free fall time. If we assume the cluster potential well is described by a NFW profile (Navarro, Frenk & White, 1996) the free fall time for a point mass at rest at a radius  $r \ll r_s$  can be well approximated by:

$$t_{ff} = \sqrt{\frac{2r}{g}}, \quad (7)$$

where  $r_s$  is the scale radius,  $g = 2\pi G \delta_c \rho_{crit}$ ,  $G$  is the Newton's constant,  $\rho_{crit} = 3H^2/8\pi G$  is the critical density for closure, and  $\delta_c$  is the characteristic density contrast. Using the best fit NFW parameters for our cluster and  $r \approx 20$  kpc we find:

$$t_{ff} \approx 108 \times h_{70}^{-1} \sqrt{\frac{r}{20 \text{ kpc}}} \text{ yr}. \quad (8)$$

From Table 3 we see that the free fall and the cooling times are similar, thus the actual sinking time is much longer than the cooling time. Therefore, unlike the first case considered above, if the ambient gas is supported by an extra non thermal pressure component such that the gas and the blobs are in pressure equilibrium, we expect the blobs to cool down before they can actually sink into cluster center. Hence, some mass deposition into a cold phase is possible.

## 6.3. Possible dynamical models

We conclude this section by discussing possible dynamical models that may explain the origin of the observed complex structure in the core of 2A 0335+096. Our starting point is the evidence for the presence of a dense gas core that moves from North to South, with a Mach number  $M \simeq 0.75 \pm 0.2$  (see §6.1).

We propose two models:

- i) the motion of the cool core induces instabilities that penetrate inside the core and disturb the gas,
- ii) the central galaxy has an intermittent AGN which makes the cool gas “bubbling”.

The features observed in the cluster result from the development of hydrodynamic instabilities induced by these two phenomena. Below we discuss in detail these two models. We conclude that both models are consistent with the available data and that further observations are required to discriminate between the two cases.

### 6.3.1. Core Destruction by Hydrodynamic Instabilities

We first show that small-scale structure can be the result of hydrodynamic instabilities induced by the observed motion of the core gas (revealed by the presence of the cold front. This motion may be due to a merger (as in A2142 or A3667, Markevitch et al. 2000; Vikhlinin et al. 2001), or due to the gas sloshing as in many other cooling flow clusters (Markevitch et

<sup>9</sup> Note that  $t_s = t_{ff}$  just in the extreme case in which we assume that both the gas is collisionless and the blob have zero angular momentum.

al. 2001, 2002). The precise nature of the core motion is not important.

The orientation of the front (see e.g. Fig.13), together with the asymmetry in the temperature distribution (see Fig.6), suggests that the core is moving along a projected direction that goes from north to south. If the core is in fact a merging subcluster, it is clear that in projection the position of the subcluster is very close to the cluster center (see §3.1), from the available data, however, we cannot measure the merger impact parameter. Hence, the subcluster may in fact be passing through the cluster at any distance along the line of sight from the center.

When a dense gas cloud is moving with respect to a rarefied one, the interface between the two gasses is subject to hydrodynamical Rayleigh-Taylor (R-T) and Kelvin-Helmholtz (K-H) instabilities. In the following we estimate the effect of both instabilities on the moving core using the same approach as Vikhlinin & Markevitch (2002). We assume that the gas cloud is a sphere of radius equal to the distance of the observed front,  $R \approx 56.7''$  ( $\approx 39.7$  kpc). As the cloud moves, the external gas flows around its border. The inflowing gas slows down at the leading edge of the sphere but reaccelerates at larger angles as it is squeezed to the sides by new portion of inflowing gas. In the case of an incompressible fluid, the velocity at the surface of the sphere is purely tangential and is given by  $v_{\text{fluid}} = 3/2v_{\infty} \sin \varphi$ , where  $v_{\infty}$  is the velocity of the inflowing gas at infinity and  $\varphi$  is the angle of the considered point on the cloud with respect to its direction of motion (see e.g. Lamb 1945). Unfortunately there is no analytic solution for the flow of a compressible fluid around a sphere. Nevertheless, the qualitative picture is similar. As we are only interested in order of magnitude estimates, in the following we parametrize the actual fluid speed introducing the parameter  $\eta$  so that:

$$v_{\text{fluid}} = \eta v_{\infty} \sin \varphi. \quad (9)$$

The parameter  $\eta$  should range between 1 (fluid velocity at the surface of the sphere equal to the inflowing gas at infinity) and 1.5 (incompressible fluid).

First we consider the R-T instability. This instability develops only if the acceleration induced by the drag force  $d_g$  is greater than the gravitational potential acceleration near the front due to the cluster mass inside the moving cloud. If we assume hydrostatic equilibrium, then the gravitational acceleration is given by:

$$g = -\frac{kT}{\mu m_p R} \left( \frac{d \log n}{d \log r} + \frac{d \log T}{d \log r} \right), \quad (10)$$

where,  $\mu m_p$  is the mean particle mass, and  $n$  and  $T$  are the gas electron density and temperature profiles, respectively. In our case this gives  $g = 1.7 \times 10^{-8}$  cm s $^{-2}$  (see §3.2, §4.4, and Fig. 4). On the other hand, the cloud acceleration due to the drag force is given

$$g_d = 0.15 \frac{n_{\text{in}}}{n_{\text{out}}} \frac{M c_s}{R}, \quad (11)$$

(where  $n_{\text{in}}, n_{\text{out}}$  the gas electron density inside and outside the edge) which in our case gives  $g_d = 2.5 \times 10^{-9}$  cm s $^{-2}$ . As the drag acceleration is less than the gravitational one, then the R-T instabilities should be suppressed.

Now we consider the K-H instability. This instability may develop whenever two fluids in contact have a non-zero tangential velocity. As for the R-T instability, the presence of a

gravitational field may suppress the development of the instability. The stability condition is such that a perturbation with wavenumber less than  $k = 2\pi/\lambda$  is stable if:

$$g \geq \frac{Dk(v)^2}{D^2 - 1} \quad (12)$$

where  $g$  is the gravitational acceleration at the interface between the two regions and  $D \equiv n_{\text{in}}/n_{\text{out}}$  is the density contrast. Using the Eq. 9 for the tangential velocity, Eq. 12 becomes:

$$\lambda \geq 2\pi \frac{D}{D^2 - 1} \frac{\eta^2 v_{\infty}^2 \sin^2 \varphi}{g} \approx 400 - 900 \sin^2 \varphi \text{ kpc.} \quad (13)$$

Eq. 13 shows that gravity suppresses instabilities only on scales larger than 400 kpc. Hence, in absence of other stabilizing mechanism, we expect the formation of the K-H instabilities on smaller scales.

In the case of 2A 0335+096, we see the instabilities on scales of the order of the radius of the sphere  $R$  may develop already at  $\varphi > 18^\circ$ . The condition that the instability on the gas cloud scale can develop, although necessary is not sufficient. In fact, in order to effectively disrupt the gas of the moving gas cloud, the growth time  $\tau$  of the instability must be much shorter than the dynamical time of the system (the cluster crossing time,  $t_{\text{cross}}$ ). We thus require (see Vikhlinin, Markevitch, & Murray 2001b, and algebraic correction of Mazzotta et al. 2002):

$$\frac{t_{\text{cross}}}{\tau} \sim 3.3 \frac{L}{\lambda} \sin \varphi \gg 1. \quad (14)$$

If we assume that the cluster radius is  $r = 1$  Mpc, at the angle at which the instability starts to develop of  $\varphi = 18^\circ$ , we find that  $t_{\text{cross}}/\tau \approx 25$ . Furthermore, at the much larger angle of  $\varphi = 90^\circ$ , where the instabilities are most effective, we find  $t_{\text{cross}}/\tau \approx 83$ . Therefore, they have sufficient time to grow to the non-linear regime.

The effect of K-H instabilities is to turbulently mix the gas in the dense moving cool cloud with the more diffuse hotter cluster gas. In particular some less dense gas from the cluster could be deposited into the denser gas cloud and vice-versa. Such a process may be responsible for the formation of the observed X-ray clumpy structure. Similarly, any pre-existing cold ( $< 30$  K) gas deposited in the cluster and/or sub-cluster core by a cooling flow will also be mixed and redistributed on these scales. This would explain the observed H $\alpha$ +[NII] emission morphology. On the other hand, these sub-sonic K-H instabilities will not produce any significant radio signature. Hence, in this scenario the radio properties of 2A 0335+096 (the mini-halo and the X-ray holes) must be related to activity of the central galaxy.

In conclusion, the observed X-ray properties of the 2A 0335+096 core may be produced by K-H instabilities induced by the motion of the core.

### 6.3.2. Gas “bubbling” by central AGN

The observed structure of 2A 0335+096 can also be accounted for if the central cluster galaxy hosts an AGN that undergoes intervals of strong activity followed by periods of relative quiescence (e.g. Binney & Tabor 1995, Soker et al. 2000). During each active period, the AGN inflates two bubbles by filling them with relativistic electrons. As observed in other clusters (e.g. Perseus, Fabian et al. 2000; Hydra A, McNamara et al. 2000; Abell 2052, Blanton et al. 2001), this expansion creates an external shell where the gas is denser. The

bubbles rise buoyantly, entrain the dense gas underneath them and induce convection (e.g., Churazov et al. 2001). These bubbles are also subjected to hydrodynamic instabilities that destroy them, fragmenting the denser shell into what we observe as denser X-ray blobs. The observed structure in the core may be created by numerous bursts of AGN activity during which the jets point in different directions. We can visualize this process as “gas bubbling” induced by the energy injection from a central AGN. The difference from other clusters with similar X-ray cavities but lacking such filamentary or blobby structure might be caused by a shorter duty cycle of the central AGN in 2A 0335+096, of the order of  $10^7$  yr (see §6.2).

The relativistic electrons produced by the AGN that are likely to be present inside the non-thermal bubbles (see e.g. McNamara 2002 and references therein) should eventually distribute in the central cluster region. However, they may avoid the densest gas blobs due to, for example, an enhanced magnetic field created during the shell compression induced by the bubble expansion. These electrons would add a non-thermal pressure component in the ambient (inter-blob) gas that may account for the apparent pressure nonequilibrium of the cluster core.

As discussed in §6.2, in this case the dense X-ray blobs have time to cool, depositing some mass in a cold phase. This cool gas may explain the presence of the observed CO and H $\alpha$ +[NII] extended emission in the cluster center (see Fig. 12).

The relativistic electrons produced by the AGN may also account for the presence of the mini radio halo observed in the cluster core (see Fig. 13).

We finally mention that there may be a connection between the AGN activity and the core sloshing, hinted at by the observed correlation between the presence of the X-ray bubbles and cold fronts in the central regions of many cooling flow clusters (Markevitch et al. 2002). Reynolds, Heinz & Begelman (2002) showed that during an AGN jet formation, a spherical pulse forms and propagates at the sound speed into the intracluster medium. Repeated AGN activity may in-

ject sufficient kinetic energy to produce sloshing of the gas, although it is unclear how the bulk motion of the core as a whole could be produced. Sloshing of the dense core may also be induced by a merger, even if the merging subcluster did not reach the center of the main cluster (e.g., Churazov et al. 2003).

To conclude this section, “gas bubbling” induced by central AGN provides a plausible explanation of the observed features in the cluster core.

## 7. CONCLUSION

The poor cluster 2A 0335+096 has several remarkable features that are only detectable with the superb resolution of *Chandra*. First, there is a cold front indicating a mildly subsonic gas motion. Second, two X-ray cavities that may be associated with steep spectrum radio emission indicating previous radio activity in this system. Third, a number of small dense gas blobs in the cluster core that may be the shreds of a cooling core disturbed either by K-H instabilities or “bubbling” induced by intermittent AGN activity. All of these properties relate to processes that may act to disrupt or destroy any cooling flow (sub-cluster merger, injection of non-thermal electrons into the intracluster medium or direct radiation from an AGN). From this relatively short X-ray observation it is not possible to determine which process (if any) dominates. Future deeper observations in the X-ray, radio and optical of 2A 0335+096 may allow the energetics of each to be assessed. When combined with observations of other similar clusters, it will be possible draw concrete conclusions about the astrophysical nature of cooling flows.

We thank David Gilbank for useful comments and suggestions and for assistance with the narrow-band optical image, Craig Sarazin for providing the VLA images, and Alexey Vikhlinin for helpful discussions. This work was supported by an RTN fellowship, CXC grants GO2-3177X and GO2-3164X, the Royal Society and the Smithsonian Institution.

## REFERENCES

Anders, E. & Grevesse, N. 1989, *Geochim. Cosmochim. Acta*, 53, 197  
 Allen, S. W., Fabian, A. C., Edge, A. C., Böhringer, H., & White, D. A. 1995, *MNRAS*, 275, 741  
 Arnaud, K. A. 1996, *ASP Conf Ser.* 101, *Astronomical Data Analysis Software and Systems V*, 5, 17  
 Bayer-Kim, C. M., Crawford, C. S., Allen, S. W., Edge, A. C., & Fabian, A. C. 2002, *MNRAS*, 337, 938  
 Blanton, E. L., Sarazin, C. L., McNamara, B. R., & Wise, M. W. 2001, *ApJ*, 558, L15  
 Blanton, E. L., Sarazin, C. L., McNamara, B. R. 2002, *ApJ*, in press, (astro-ph/0211027)  
 Buote, D.A. 2000, *ApJ*, 539, 172  
 Cash, W. 1979, *ApJ*, 228, 939  
 Cavaliere, A. & Fusco-Femiano, R. 1976, *A&A*, 49, 137  
 Churazov, E., Brüggen, M., Kaiser, C. R., Böhringer, H., & Forman, W. 2001, *ApJ*, 554, 261  
 Churazov, E., Forman, W., Jones, C., & Böhringer, H. 2003, *ApJ*, submitted (astro-ph/0301482)  
 Cooke, B. A. et al. 1978, *MNRAS*, 182, 489  
 David, L. P., Nulsen, P. E. J., McNamara, B. R., Forman, W., Jones, C., Ponman, T., Robertson, B., Wise, M. 2000, *ApJ*, 557, 546  
 Dickey, J. M. & Lockman, F. J. 1990, *ARA&A*, 28, 215  
 Edge, A. C., Stewart, G. C., Fabian, A. C., & Arnaud, K. A. 1990, *MNRAS*, 245, 559  
 Edge, A. C. 2001, *MNRAS*, 328, 762  
 Fabian, A. C. 1994, *ARA&A*, 32, 277  
 Fabian, A. C. et al. 2000, *MNRAS*, 318, L65  
 Fabian, A. C., Sanders, J. S., Ettori, S., Taylor, G. B., Allen, S. W., Crawford, C. S., Iwasawa, K., & Johnstone, R. M. 2001, *MNRAS*, 321, L33  
 Forman, W., Jones, C., Markevitch, M., Vikhlinin, A., & Churazov, E. 2002, *ASSL Vol. 272: Merging Processes in Galaxy Clusters*, 109  
 Glenn Morris, R. & Fabian, A. C. 2003, *MNRAS*, 338, 824  
 Huchra, J. P., Wyatt, W. F., & Davis, M. 1982, *AJ*, 87, 1628  
 Irwin, J. A. & Sarazin, C. L. 1995, *ApJ*, 455, 497  
 Johnstone, R. M., Allen, S. W., Fabian, A. C., & Sanders, J. S. 2002, *MNRAS*, 336, 299  
 Kaastra, J.S. 1992, *An X-Ray Spectral Code for Optically Thin Plasmas* (Internal SRON-Leiden Report, updated version 2.0)  
 Kaastra, J. S., Ferrigno, C., Tamura, T., Paerels, F. B. S., Peterson, J. R., & Mittaz, J. P. D. 2001, *A&A*, 365, L99  
 Kikuchi, K., Furusho, T., Ezawa, H., Yamasaki, N. Y., Ohashi, T., Fukazawa, Y., & Ikebe, Y. 1999, *PASJ*, 51, 301  
 Lamb, H. 1945, *Hydrodynamics* (New York: Dover)  
 Liedahl, D.A., Osterheld, A.L., and Goldstein, W.H. 1995, *ApJ*, 438, L115  
 Markevitch, M., Ponman, T. J., Nulsen, P. E. J., Bautz, M. W., Burke, D. J., David, L. P., Davis, D., Donnelly, R. H., Forman, W. R., Jones, C., Kaastra, J., Kellogg, E., Kim, D.-W., Kolodziejczak, J., Mazzotta, P., Pagliaro, A., Patel, S., VanSpeybroeck, L., Vikhlinin, A., Vrtilek, J., Wise, M., Zhao, P. 2000b, *ApJ*, 541, 542  
 Markevitch, M., Vikhlinin, A., & Mazzotta, P. 2001, *ApJ*, 562, L153  
 Markevitch, M., Vikhlinin, A., Forman, W. R. 2002: *Matter and Energy in Clusters of Galaxies*, Taiwan, in press (astro-ph/0208208)  
 Markevitch, M., et al. 2003, *ApJ*, 583, 70  
 Mazzotta, P., Markevitch, M., Vikhlinin, A., Forman, W. R., David, L. P., & VanSpeybroeck, L. 2001, *ApJ*, 555, 205  
 Mazzotta, P., Fusco-Femiano, R., & Vikhlinin, A. 2002, *ApJ*, 569, L31  
 McNamara, B. R., O'Connell, R. W., & Bregman, J. N. 1990, *ApJ*, 360, 20

McNamara, B. R. & O'Connell, R. W. 1992, *ApJ*, 393, 579

McNamara, B. R. et al. 2000, *ApJ*, 534, L135

McNamara, B. R. 2002, *ASP Conf. Ser.* 262: The High Energy Universe at Sharp Focus: *Chandra Science*, 351, (astro-ph/0202199)

Molendi, S. & Gastaldello, F. 2001, *A&A*, 375, L14

Molendi, S. & Pizzolato, F. 2001, *ApJ*, 560, 194

Navarro, J. F., Frenk, C. S., & White, S. D. M. 1996, *ApJ*, 462, 563

Paturel, G., Fouque, P., Bottinelli, L., & Gouguenheim, L. 1989, *A&AS*, 80, 299

Peterson, J. R. et al. 2001, *A&A*, 365, L104

Reynolds, C. S., Heinz, S., & Begelman, M. C. 2002, *MNRAS*, 332, 271

Romanishin, W. & Hintzen, P. 1988, *ApJ*, 324, L17

Sanders, J. S. & Fabian, A. C. 2002, *MNRAS*, 331, 273

Sarazin, C. L., O'Connell, R. W., & McNamara, B. R. 1992, *ApJ*, 397, L31

Sarazin, C. L., Baum, S. A., & O'Dea, C. P. 1995, *ApJ*, 451, 125

Schmidt, R. W., Fabian, A. C., & Sanders, J. S. 2002, *MNRAS*, 337, 71

Schwartz, D. A., Schwarz, J., & Tucker, W. 1980, *ApJ*, 238, L59

Singh, K. P., Westergaard, N. J., & Schnopper, H. W. 1986, *ApJ*, L308, L51

Singh, K. P., Westergaard, N. J., & Schnopper, H. W. 1988, *ApJ*, 331, 672

Taylor, G. B., Fabian, A. C., & Allen, S. W. 2002, *MNRAS*, 334, 769

Tamura, T. et al. 2001, *A&A*, 365, L87

Vikhlinin, A., Forman, W., & Jones, C. 1999, *ApJ*, 525, 47

Vikhlinin, A., Markevitch, M., Murray, S.S. 2001a, *ApJ*, 551, 160

Vikhlinin, A., Markevitch, M., Murray, S.S. 2001b, *ApJL*, 549, L47

Vikhlinin, A. A. & Markevitch, M. L. 2002, *Astronomy Letters*, 28, 495

Voigt, L. M., Schmidt, R. W., Fabian, A. C., Allen, S. W., & Johnstone, R. M. 2002, *MNRAS*, 335, L7

White, D. A., Fabian, A. C., Johnstone, R. M., Mushotzky, R. F., & Arnaud, K. A. 1991, *MNRAS*, 252, 72

Wilms, J., Allen, A., & McCray, R. 2000, *ApJ*, 542, 914

Young, A. J., Wilson, A. S., & Mundell, C. G. 2002, *ApJ*, 579, 560